


Nonreciprocal spin-wave transport in an asymmetric three-dimensional magnonic coupler

A.A. Grachev¹,* S.A. Odintsov¹, E.N. Beginin, and A.V. Sadovnikov¹
Laboratory "Metamaterials", Saratov State University, Saratov 410012, Russia

 (Received 21 July 2023; revised 4 December 2023; accepted 5 January 2024; published 15 February 2024)

Here, we present a study investigating the effects of spin-wave coupling in a structure composed of parallel-oriented magnonic stripes fabricated from thin films of yttrium-iron garnet. The structure consists of two parallel stripes separated by a sufficiently small gap to enable dipolar coupling, while a third stripe is positioned atop the lateral system, forming an asymmetric three-dimensional (3D) coupler geometry. Through the utilization of Brillouin light-scattering spectroscopy, we experimentally demonstrate the transport of spin waves along the asymmetric 3D coupler. Additionally, by employing experimental techniques, we explore the nonreciprocal propagation of spin waves in the considered structure by reversing the polarity of the external magnetic field. To gain further insights, we employ micromagnetic modeling and the finite-element method to obtain the eigenmode spectra of the asymmetric 3D coupler. Our results show that reversing the polarity of the external magnetic field induces coupling between the magnetic stripes. We elucidate the characteristics of lateral and vertical spin-wave transport, as well as nonreciprocal spin-wave propagation within the investigated structure. Notably, in the asymmetric 3D coupler, the coupling length diminishes, offering the potential to enhance the density of functional elements in the design of three-dimensional magnonic networks.

DOI: [10.1103/PhysRevApplied.21.024031](https://doi.org/10.1103/PhysRevApplied.21.024031)

I. INTRODUCTION

The use of elementary quanta of magnetic excitations [magnons or spin waves (SWs)] as carriers of information signals has recently attracted more and more interest due to the possibility of transferring the magnetic moment (spin) of the electron without transferring the electric charge and thus without heat generation inherent in CMOS technology [1–7]. The properties of SWs are determined by dipole and exchange interactions in magnetic media [8–10] and can change significantly when magnetic films are patterned. SWs have applications related to generation, [11] transmission [12,13], and signal processing [14–17] at the micro- and nanoscale magnetic structures.

The fabrication of elementary blocks that perform a given set of signal-processing functions (multiplexing and demultiplexing [18–20], signal splitting [21–23], spatial frequency selection [24,25]), linear and nonlinear switching [22,26,27]), leads to the design of interconnects for efficient spin-wave transfer within magnonic networks [28–31], which are a topology of coupled micro- and nanoscale magnetic structures. Magnonic networks play a key role in the development of another generation of functional devices for microwave and terahertz information

and telecommunication systems based on magnonics principles [3,4].

Spin-wave dipole coupling effects in multilayer [32,33] and lateral [21,23] structures can be used in the design of magnonic networks based on lateral microstructures to suppress the cross signal between neighboring elements. At the same time, spin-wave coupling effects can be used to realize spatial-frequency selection modes of SWs [34] and to create interconnection elements within magnonic networks [21,25,26] in the vertical and lateral directions. The use of alternative physical phenomena arising from the propagation of signals in three-dimensional periodic and irregular structures significantly expands the functionality of information processing systems [28,35,36]. At the same time, the question of the fabrication of three-dimensional magnonic networks, which allow the transmission of SWs simultaneously in lateral and vertical directions, remains open. This approach will provide an opportunity to increase the density of spatial packing of basic elements for the construction of scalable three-dimensional (3D) magnonic networks [37–39] and also to reduce the total length of connections between elements. This approach makes it possible to create multilevel arrays of waveguide magnetic stripes and transmit the spin-wave signal in three dimensions. The use of the third dimension in these multilevel waveguide system allows for the crossing-free routing of multiple spin-wave flows

*Andrew.A.Grachev@gmail.com

in a magnonic integrated circuit. In addition, 3D micro- and nano-objects exhibit unusual properties compared to planar magnetic structures: chirality, nonreciprocity, etc.

Nonreciprocal spin-wave propagation in magnonic structures has gained significant relevance in recent years due to its unique properties and potential applications [33, 40–44]. Nonreciprocity refers to the asymmetric behavior of spin waves, where their propagation is allowed in one direction while being blocked or suppressed in the opposite direction. This characteristic opens up alternative avenues for the development of advanced magnonic devices with enhanced functionality and performance [42,43]. Nonreciprocal propagation [40,45–49] of SWs in magnetic waveguides can be observed in a tangential magnetized configuration (when the direction of the wave vector and the magnetization are perpendicular to each other in the film plane). In this case, the eigenmodes of the counter-propagating SWs can differ significantly due to different magnetic surface anisotropies at the two film surfaces [48]. For multilayer waveguides, the classical object demonstrating nonreciprocity is a structure of two similar layers with antiparallel orientation of magnetization [40,45]. Until now, the effect of nonreciprocal spin-wave propagation has only been considered for metallic magnetic waveguides [47] or for multilayer waveguides with different values of saturation magnetization [48]. In this case, these changes in the magnetic media create regions of nonreciprocal wave propagation.

In this paper, we propose a three-dimensional magnonic structure based on lateral magnonic stripes with an overlying magnonic stripe. Using Brillouin light-scattering spectroscopy, we have experimentally demonstrated spin-wave transport along the asymmetric 3D coupler. The nonreciprocal nature of the distribution of the dynamic magnetic fields and the nonreciprocal dispersion characteristics of the waves propagating in opposite directions in the structure allow the spatial 3D separation of the spin-wave beams for different frequencies of the carrier signals, opening up other possibilities for 3D spatial multiplexing and demultiplexing.

II. 3D MAGNONIC COUPLER AND MICROMAGNETIC CALCULATIONS

Figure 1(a) shows schematically the considered structure, which is a system of parallel-oriented magnonic stripes fabricated from yttrium-iron-garnet film [YIG, $\text{Y}_3\text{Fe}_5\text{O}_{12}$ (111)], $t = 10 \mu\text{m}$ -thick and saturation magnetization $M_0 = 139 \text{ G}$, grown on a 500- μm -thick gadolinium-gallium garnet [GGG, $\text{Gd}_3\text{Ga}_5\text{O}_{12}$ (111)] substrate. The YIG stripes are labeled S_1 , S_2 , and S_3 and have equal widths $w = 200 \mu\text{m}$. The distance between S_1 and S_2 is $d = 40 \mu\text{m}$. The distance s between the stripes $S_{1,2}$ and S_3 stripe is varied from 10 to 80 μm [see inset in Fig. 1(a)]. The length along the long side of the magnonic stripes was

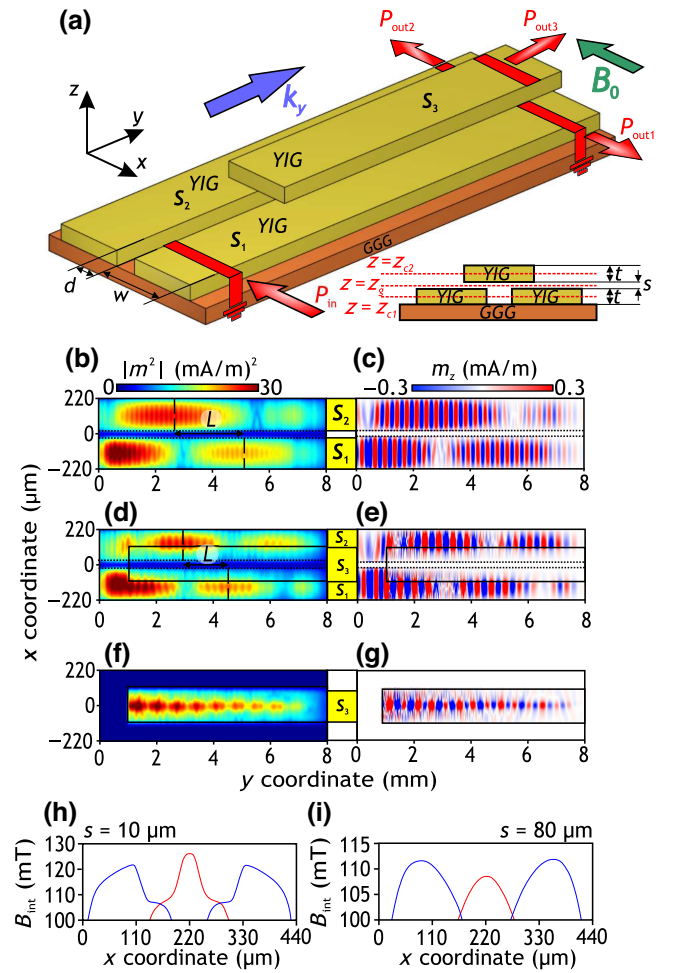


FIG. 1. (a) Schematic of the investigated structure. The inset shows the x - z plane. (b)–(g) The left panels show simulated distributions of the spin-wave intensity proportional to the magnitude of the square of the dynamic magnetization, the right panels show simulated distributions of the dynamic magnetization component m_z . Case of two magnonic stripes (b),(c) and 3D coupler (d)–(g). The data are given for $B_0 = 120 \text{ mT}$ and the input frequency $f = 5.3 \text{ GHz}$. Profiles of the internal magnetic field of the magnonic stripes $S_{1,2}$ (blue curves) and S_3 (red curves) for $s = 10 \mu\text{m}$ (i) and $s = 80 \mu\text{m}$ (h).

8 mm for $S_{1,2}$ and 7 mm for S_3 . The structure is placed on a microstrip transmission line in a homogeneous static magnetic field of $B_0 = 120 \text{ mT}$ directed along the x axis. This configuration allows the efficient excitation of surface magnetostatic waves (MSSWs) [50]. The excitation of MSSWs propagating along the positive direction of the y axis occurs in the S_1 magnonic stripe.

It should be noted that when studying the propagation of SWs in transversely coupled structures, it is important to take into account the demagnetizing internal magnetic fields. A numerical simulation has been performed based on the solution of the Landau-Lifshitz-Hilbert equation

[51] (LLG) by the Dorman-Prins method [25,52]:

$$\frac{\partial \mathbf{M}}{\partial t} = \gamma [\mathbf{B}_{\text{eff}} \times \mathbf{M}] + \frac{\alpha}{M_0} \left[\mathbf{M} \times \frac{\partial \mathbf{M}}{\partial t} \right], \quad (1)$$

where \mathbf{M} is the magnetization vector, $\gamma = 28$ GHz/T is the gyromagnetic ratio, $\alpha = 10^{-5}$ is the damping parameter, $\mathbf{B}_{\text{eff}} = \mathbf{B}_0 + \mathbf{B}_{\text{demag}} + \mathbf{B}_{\text{ex}} + \mathbf{B}_a$ is the effective magnetic field, \mathbf{B}_0 is the external magnetic field, $\mathbf{B}_{\text{demag}}$ is the demagnetization field, \mathbf{B}_{ex} is the exchange field, \mathbf{B}_a is the anisotropy field. The parameter of the exchange constant in YIG film was $A_{\text{ex}} = 3.612$ pJ/m. To reduce the reflection of the signal from the boundaries of the calculation region ($y = 0$ and $y = 8$ mm), regions ($0 < y < 0.5$ mm and $7.5 < y < 8$ mm) with a geometrically increasing α factor were introduced in the calculation. The mesh was set at $5 \times 3 \times 2 \mu\text{m}^3$ since the SW dynamics was not affected by exchange interaction and the shortest SW wavelength was $10 \mu\text{m}$.

To excite the propagating SWs, a sinusoidal magnetic field $b = b_0 \sin(2\pi ft)$ was applied to a $100\text{-}\mu\text{m}$ -long section with different oscillation amplitude b_0 and frequency f . $M_z(x, y, t)$ of each cell was recorded for 300 ns, enough to reach a steady state. The oscillations $m_z(x, y, t)$ were calculated for all cells using the formula $m_z(x, y, t) = M_z(x, y, t) - M_z(x, y, 0)$, where $M_z(x, y, 0)$ corresponds to the ground state.

Figures 1(b), 1(d), and 1(f) show the results of micromagnetic simulation of the spin-wave intensity distribution proportional to the magnitude of the square of the dynamic magnetization $I(x, y, z) = m_y^2 + m_z^2$. Figures 1(c), 1(e), and 1(g) show the distribution of the dynamic magnetization component m_z . Figures 1(b) and 1(c) show the case for two lateral magnetic stripes S_1 and S_2 , it can be seen that the spin-wave power is transferred from S_1 to S_2 for a distance along the y axis equal to the coupling length L (indicated in figures), which is equal to the distance at which the spin-wave energy is transferred from stripe S_1 to stripe S_2 . It is worthwhile to note that throughout the research in this paper, we will treat L as the coupling length in the S_1 and S_2 stripes. In the case of a system of three magnonic stripes [see Figs. 1(d)–1(g)], it can be seen that for a fixed input frequency $f = 5.3$ GHz, the coupling length L changes by an order of magnitude $L/\sqrt{2}$ compared to the case of two lateral magnetic stripes [53], due to changes in both the equilibrium magnetization distribution and the spin-wave signal transfer.

The calculation of the internal demagnetization fields in the lateral layered microstructure was then carried out. Figures 1(h) and 1(i) show the internal magnetic field profiles of the magnonic stripes $S_{1,2}$ (blue curves) and S_3 (red curves) in the cross sections along x axis [see inset in Fig. 1(a)] in $z = z_{c1}$ for $S_{1,2}$ and in $z = z_{c2}$ for S_3 . These positions correspond to the central point of all stripes when the gap value s is varied. It can be seen that at gap $s =$

$10 \mu\text{m}$ [see Fig. 1(h)] there is a strong transformation of the $B_{\text{int}}(x)$ profiles in all three stripes. At the same time, an asymmetry in the distribution of the internal magnetic field is observed on stripes S_1 and S_2 , in the region above stripe S_3 . This asymmetry in the $B_{\text{int}}(x)$ distribution does not prevent SWs from being transferred to each of the magnetic stripes. Note that at the gap $s = 80 \mu\text{m}$ the value of B_{int} in the center of each magnonic stripe becomes more homogeneously compared to the case with $s = 10 \mu\text{m}$. We will refer to this geometry as an asymmetric 3D coupler. Let us add that the term ‘‘asymmetric’’ here means the asymmetric arrangement of the stripe S_3 above each of the stripes S_1 and S_2 and the creation of an asymmetric internal magnetic field distribution profile in them.

It should be noted that electromagnetic waves propagating in guided structures with gyrotropic media have the property of nonreciprocity—dependence of the wave-number value on the direction of propagation. And if we add another stripe on top of the two lateral stripes, it will cause asymmetry in the internal magnetic field distribution and lead to the manifestation of nonreciprocal spin-wave propagation in a considered 3D coupler. Therefore, dispersion characteristics have been calculated using micromagnetic modeling. From these calculations we see that the $S_{1,2}$ [see Figs. 2(a) and 2(b)] stripes have three pronounced modes in the spin-wave spectra. At the same time, for the S_3 stripe [see Fig. 2(c)], only two pronounced modes are observed in the spectrum. A more detailed description of these modes will be considered later. The dashed lines are approximations of the obtained dispersions. Red ovals mark the areas of the significant variations of the dispersion. For example, the slope of the dispersion in the high-frequency range for negative k changes for stripe S_1 . For stripes $S_{2,3}$, a frequency shift of the dispersion curves is observed, as well as a change in their slope. In the positive wave-number region at frequencies around 5.4 GHz, hybridization of waves propagating in the $S_{1,2}$ and S_3 stripes is observed. And in the negative wave-number region, this effect does not manifest itself.

If we look at the dispersion curves in the region of negative wave numbers, their slope is different from the dispersion curves in the region of positive wave numbers. This fact indicates nonreciprocal spin-wave propagation in the considered structure. To further illustrate the nonreciprocal spin-wave propagation in an asymmetric 3D coupler, the power spectral density was calculated. For this purpose the input signal was given as $b_z(t) = b_0 \text{sinc}(2\pi f_c t)$ with the centre frequency $f_c = 7$ GHz, $b_0 = 0.1$ mT. Then the dynamic magnetization value $m_z(x, y, t)$ in the output section region $P_{\text{out}1,2,3}$ was recorded in $\Delta t = 75$ fs steps for the time $T = 500$ ns. As a result, the frequency dependence of the dynamic magnetization at the outputs $P_{\text{out}1,2,3}(f)$ could be plotted using the double Fourier transform [54].

Figures 2(d)–2(f) show the frequency spectra of the spin-wave signal in the output sections of the stripes S_1

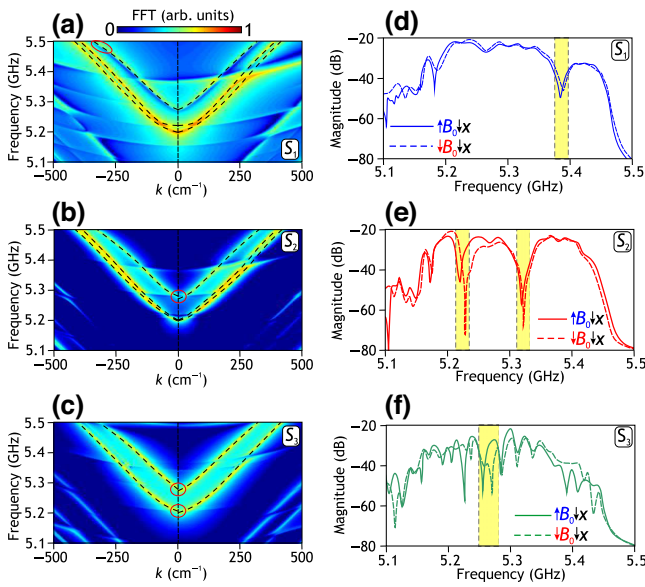


FIG. 2. Calculations of spin-wave dispersion for stripes S_1 (a), S_2 (b), and S_3 (c). Calculations of frequency dependencies of the output power in the stripes S_1 (d), S_2 (e), and S_3 (f) for the cases of the external magnetic field direction in the negative (solid curves) and the positive directions (dashed curves) of the x axis.

[see Fig. 2(d)], S_2 [see Fig. 2(e)], and S_3 [see Fig. 2(f)], for the cases of negative direction of the external magnetic field of the x axis (solid curves) and positive direction of the x axis (dashed curves). It is elucidated in Appendix A how the spectra are transformed when the field is rotated by 180° due to symmetry breaking, while, if we consider the case of two lateral stripes, the rotating external magnetic field does not change the transfer characteristics of the lateral stripes. In comparison with two lateral magnonic stripes the proposed 3D coupler demonstrates nonreciprocal spin-wave transmission. The polarity reversal of the external magnetic field results in a redistribution of the spin-wave signal power in all magnonic stripes into areas of frequency dips [see yellow areas in Figs. 2(d)–2(f)] corresponding to the transfer of spin-wave power between the magnetic stripes. The largest change in the redistribution of spin-wave power is observed in the S_2 stripe [see Fig. 2(e)], where there is a frequency shift of 15 MHz in these dips. It can be seen that for the stripe S_2 , the polarity reversal of the external magnetic field produces a large frequency dip in spin-wave power (of about 20 dB) in the range from 5.22 to 5.24 GHz. This fact demonstrates the good tunability of the proposed 3D coupler configuration by simply changing the polarity of the external magnetic field.

It should also be noted that the observing of nonreciprocal spin-wave propagation can be related to two facts. The first is the highly inhomogeneous asymmetric distribution of the internal magnetic field generated by the stripe S_3 . The second is the presence of a distributed dipolar coupling between the magnetic stripes in the lateral and

vertical directions, which leads to a change in the trajectory of the magnetic moment precession [44] and the ellipticity [55] of the spin-precession motion across the width of the magnetic stripes.

III. EXPERIMENTAL OBSERVATION OF SPIN-WAVE PROPAGATION IN AN ASYMMETRIC 3D COUPLER

A. Description and preparation of experimental measurements

To confirm the micromagnetic simulation results, an experimental study of the SW propagation in the proposed 3D coupler was carried out using the Brillouin light-scattering spectroscopy [56,57] (BLS) technique in the backscattering configuration. A simplified schematic representation of this experimental setup is shown in Fig. 3(a). In quantum mechanical terms, where light quanta are represented by photons and a magnon is a spin-wave excited quasiparticle, the BLS process can be described by the

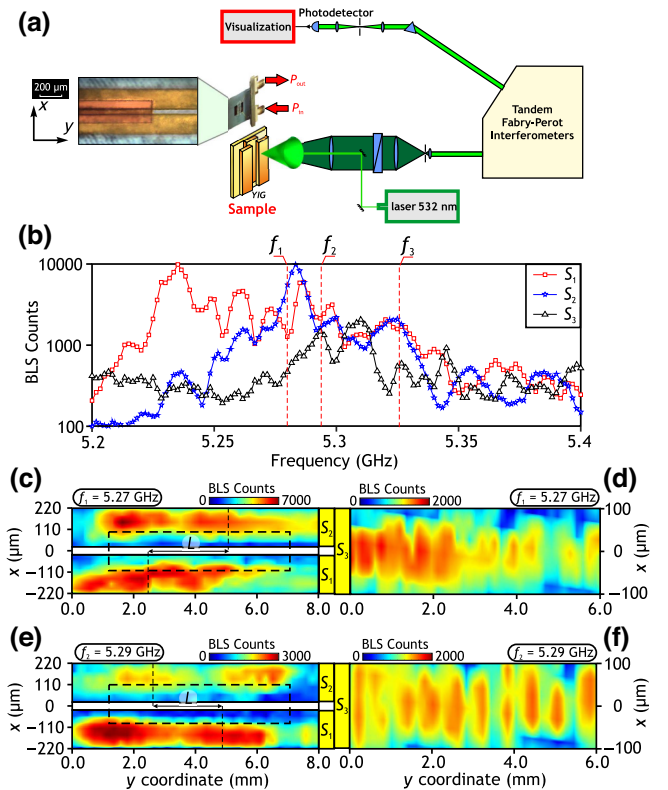


FIG. 3. (a) Schematic of the BLS setup, containing a photograph of the 3D asymmetric coupler layout and a micrograph of the coupled magnetic stripes. (b) Frequency dependence of the BLS signal in stripes S_1 (red curve), S_2 (blue curve), and S_3 (black curve), measured experimentally on a fabricated setup using the BLS technique. BLS intensity 2D spatial maps obtained in stripes S_1 and S_2 (c),(e) and in stripe S_3 (d),(f), at excitation frequencies: $f_1 = 5.27$ GHz (c),(d) and $f_2 = 5.29$ GHz (e),(f).

inelastic scattering of photons on magnons. The inelastically scattered light is generated by a single-frequency laser.

In general, the intensity of a BLS signal is directly proportional to the laser power applied. However, especially in BLS microscopy, the maximum laser power is limited. Due to the focusing of the laser radiation we use, local heating of the sample surface can affect the magnetization dynamics under investigation. In our case, a single-mode Excelsior solid-state laser (EXLSR-532-50-CDRH) was used to generate the P -polarized green light. The laser beam was focused on the surface of the YIG film using a Nikkor lens with a numerical aperture of 1.2 and a focal length of 50 mm. The scattered light was collected with the same lens. To determine the magnon contribution to the inelastic scattered light signal, a method was used to suppress signals from elastically scattered photons and surface photons scattered by phonons [58]. The setup includes a set of two tandem Fabry-Perot interferometers consisting of two highly reflective parallel mirrors. Light passes through them only when the distance between the mirrors is a multiple of half its wavelength, while transmission is strongly suppressed for other distances between the mirrors. Spin-wave intensity $I_{\text{BLS}}(x, y)$ in the structure scanned by a probing light spot over a stripe region with a spatial resolution of 25 μm .

In the experiment, spin-wave excitation was performed in a stripe S_1 by an gold microstrip antenna 1 μm thick and 30 μm wide, which placed at the Al_2O_3 layer, which is used for a standard 50- Ω microstrip line. A microwave signal with power $P_{\text{in}} = -15$ dBm from a synthesized CW generator (Anritsu MG3692C) was applied to the input antenna. The spacing between stripes $S_{1,2}$ and S_3 was provided by a 10 μm layer of mica.

B. Discussion of experimental measurements

Figure 3(b) shows the frequency dependence of the I_{BLS} dynamic magnetization intensity at $x = 6.0$ mm at the output of each of the S_j magnonic stripes ($j = 1, 2, 3$) obtained by the BLS technique. It can be seen that the spin-wave spectrum in stripe S_3 is shifted to the high-frequency region, as in the numerical simulation. At the same time, pronounced dips in the power of the spin-wave signal are observed in each of the stripes, indicating power transfer between the magnonic stripes. To confirm this, we constructed BLS maps of the spin-wave intensity at a fixed frequencies: $f_1 = 5.27$ GHz [see Figs. 3(c) and 3(d)] and $f_2 = 5.29$ GHz [see Figs. 3(e) and 3(f)], measured on the side of S_1 and S_2 [see Figs. 3(c) and 3(e)] and on the side of stripe S_3 [see Figs. 3(d) and 3(f)]. It should be noted that there is a good qualitative agreement with the results of the micromagnetic modeling. According to Fig. 3(b), at frequency f_1 , the case is observed that corresponds to the regime where the spin-wave energy is output from the

stripe S_2 [see Fig. 3(c)]. At the same time, the significantly smaller part of the spin-wave energy is transferred to the stripe S_3 [see Fig. 3(d)]. On the spatial maps for stripes $S_{1,2}$, as well as in the micromagnetic modeling, we have indicate the coupling length L . As can be seen, at this frequency its value is $L = 2.2$ mm. For the frequency f_2 [see Figs. 3(e) and 3(f)], the same regime is observed when the maximum of the spin-wave power transferred in the stripe S_1 . At the same time, at this frequency, a picture similar to that of the micromagnetic model is observed. The coupling length at this frequency is $L = 1.7$ mm.

Moving on to study the nonreciprocal spin-wave propagation in the 3D coupler, Figs. 4(a) and 4(b) show the BLS intensity maps of the spin waves at a fixed frequency $f = 5.33$ GHz, for the cases of the external magnetic field is directed in the negative [see Fig. 4(a)] and positive [see Fig. 4(b)] direction of the x axis. It can be seen that switching the polarity of the external magnetic field causes the wave to start propagating on the different side of magnonic stripe where there is a sharp change in the internal magnetic field distribution, leading to a deterioration in the spin-wave signal propagation [see Fig. 4(b)]. Note that in this configuration of the 3D coupler, the BLS technique does not allow full quantification of the intensity

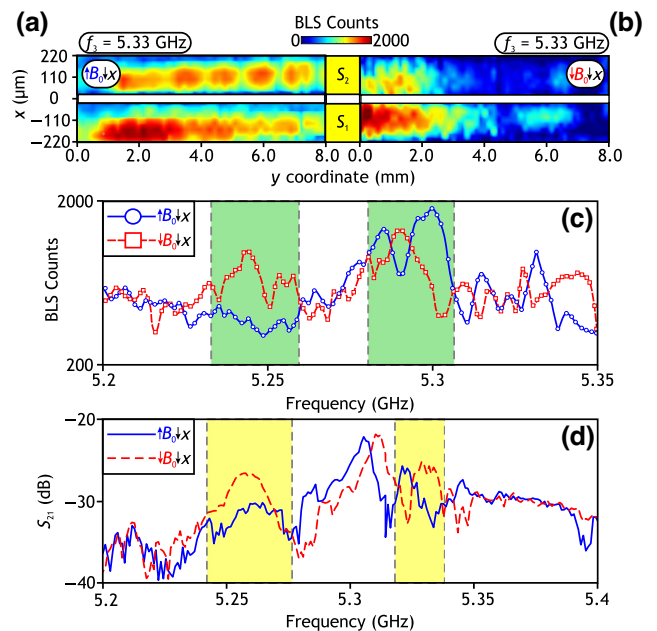


FIG. 4. BLS intensity 2D spatial maps, for cases where the external magnetic field is directed in the negative (a) and positive (b) direction of the x axis at frequency $f_3 = 5.33$ GHz. (c) The BLS frequency spectra for the stripe S_3 in cases where the external magnetic field is directed in the negative (blue circles) and positive (red squares) direction of the x axis. (d) The spin-wave transmission spectra for the stripe S_1 in cases where the external magnetic field is directed in the negative (blue solid curve) and positive (red dashed curve) direction of the x axis.

distribution in the magnonic stripes S_1 and S_2 compared to the magnonic stripe S_3 . However, it is possible to estimate the nonreciprocity in the S_3 stripe. Figure 4(c) shows the frequency dependence of the BLS counts in the S_3 stripe at positive (red squares) and negative (blue circles) orientations of the external magnetic field. In the plot, two frequency regions are shaded in green. They indicate the regions of interest where the largest variations between the amplitude-frequency characteristics are observed for different polarities of the external magnetic field.

It should be noted that a key aspect is the evaluation of the spin-wave transmission characteristics along the lateral stripe paths when nonreciprocity is present in the system. The blue solid curves in Fig. 4(d) show the transmission (S_{21}) of the MSSW measured with an Agilent Technologies E8362C vector-network analyzer for the case where the input and output microstrip transducers are placed on the stripe S_1 at a distance of 8 mm from each other. It can be seen that there are frequency dips in the transmission spectra corresponding to the coupling of the SW to the other stripe. When the external magnetic field is rotated by 180° [red dashed curve in Fig. 4(d)], we obtain a narrowing of the transmission and a frequency shift of the spin-wave power dips. From a physical point of view, this effect may be due to a change in the coupling between the magnetic stripes. This is manifested by the mode transformation, which we will discuss in the next section of the paper. It should also be noted that the mode transformation, in particular, leads to a change in the vertical coupling coefficient used in the analytical coupled wave model.

IV. FEM CALCULATION OF EIGENMODE SPECTRA AND COMPARISON WITH ANALYTICAL MODEL

Since the micromagnetic modeling method does not provide information on the spectrum of the eigenmodes of the SWs propagating in the structure formed by the YIG stripes, we calculated the electrodynamic properties of the lateral layered structure using the finite-element method (FEM). When modeling in the frequency domain, all components of the electromagnetic field depend on the frequency according to the law $e^{i\omega t}$. In this case, Maxwell's equations for the electric field strength vector \mathbf{E} give the equation

$$\nabla \times (\hat{\mu}^{-1} \nabla \times \mathbf{E}) - k^2 \varepsilon \mathbf{E} = 0, \quad (2)$$

where $k = \omega/c$ is the wave number in vacuum, $\omega = 2\pi/f$ is the circular frequency, f is the electromagnetic wave frequency, $\varepsilon = 14$ is the effective value of dielectric permittivity for YIG stripes.

The following parameters were used in the simulation: the dielectric permittivities of the GGG substrate and the YIG stripes were assumed equal to $\varepsilon_{\text{GGG}} = 9$

and $\varepsilon_{\text{YIG}} = 14$, respectively, and the magnetic permeability tensor $\hat{\mu}(f)$ of the YIG stripes was set in the form:

$$\hat{\mu}(f) = \begin{vmatrix} 1 & 0 & 0 \\ 0 & \mu(f) & \mp i\mu_a(f) \\ 0 & \pm i\mu_a(f) & \mu(f) \end{vmatrix},$$

$$\mu(f) = \frac{f_\perp^2 - f^2}{f_H^2 - f^2}, \quad \mu_a(f) = \frac{f_M f}{f_H^2 - f^2},$$

where $f_M = \gamma 4\pi M_0 = 4.9$ GHz, $f_H = \gamma B_0 = 3.36$ GHz, $f_\perp = \sqrt{f_H(f_H + f_M)} = 5.26$ GHz is the frequency of transverse ferromagnetic resonance in the tangentially magnetized ferrite film.

The eigenmode spectrum of the 3D coupler consists of an orthogonal system of two symmetric [see Figs. 5(a), 5(c), 5(d), and 5(f)] and one antisymmetric mode [see Figs. 5(b) and 5(e)] with corresponding wave numbers Φ_{S_1} , Φ_{S_2} , and Φ_{AS} . If the polarity of the external magnetic field is reversed, the mode distributions [see Figs. 5(d)–5(f)] are localized in the region $z = z_g$ [see inset

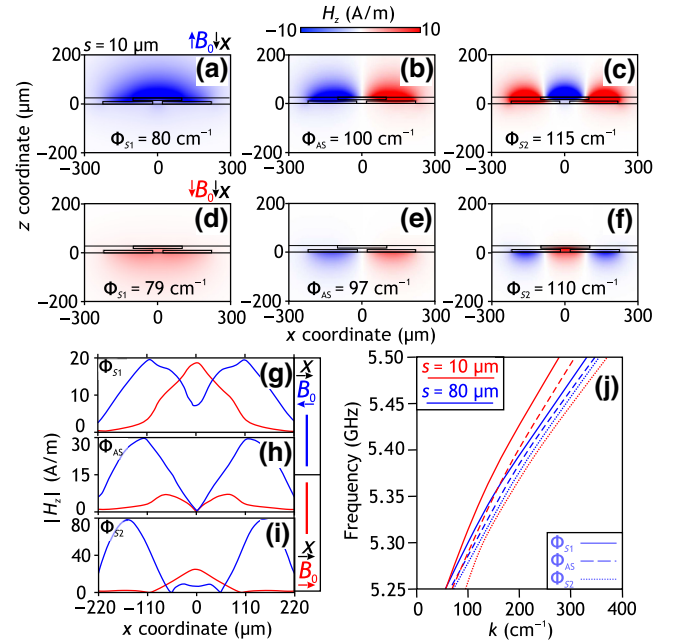


FIG. 5. (a)–(f) Distributions of the H_z magnetic field component for the eigenmodes of the 3D coupler, for cases where the external magnetic field is directed in the negative (a)–(c) and positive (d)–(f) direction of the x axis. The figures indicate the wave-number values for each eigenmode. The data are given for $B_0 = 120$ mT and input signal frequency $f = 5.3$ GHz. $|H_z|$ distribution for eigenmodes Φ_{S_1} (g), $\Phi_{S_{AS}}$ (h), and Φ_{S_2} (i) in the section along the x axis at point $z = z_g$, for cases where the external magnetic field is directed in the negative (blue curves) and positive (red curves) direction of the x axis. (j) Dispersions of the 3D coupler eigenmodes for two values of vertical gap $s = 10$ μm and $s = 80$ μm .

in Fig. 1(a)], which corresponds to a midposition of s . The distributions are localized on opposite sides of the magnetic strips and also change their sign. The modes of stripe S_3 are localized in the region of the gap s and the modes of strip $S_{1,2}$ are localized in the GGG substrate. The wave-number values for all modes also change. There is also a relative change in intensity between the S_1 , S_2 , and S_3 , as all six distributions are plotted on the same H_z scale. We can estimate the magnitude of the localization of the modes in the region of gap s when the polarity of the external magnetic field changes. For this purpose, the $|H_z|$ distributions for the modes Φ_{S_1} , Φ_{AS} , and Φ_{S_2} are shown in Figs. 5(g)–5(i), respectively. These data show that the change in polarity of B_0 from negative to positive leads to a decrease in intensity in the gap region for modes Φ_{AS} and Φ_{S_2} . These results, which indicate a change in spin-wave energy and eigenmode wave numbers, lead to a change in spin-wave dispersion in general, in good agreement with experimental and micromagnetic modeling results.

Next, it is worthwhile to evaluate the effect of the value of the gap s on the dispersion of SWs in the 3D coupler. Figure 5(j) shows the dispersions of the eigenmodes: Φ_{S_1} , Φ_{AS} , and Φ_{S_2} . Changing the gap value s leads to a transformation of the dispersion characteristics of the eigenmodes: as s decreases, the dispersion characteristics are pushed apart, which in turn leads to a decrease in coupling length. It should be noted that changing the gap makes only a significant difference for the modes Φ_{S_1} and Φ_{S_2} , as for the Φ_{AS} changing the gap does not make such a big difference in the wave numbers.

For comparison with previous results, we can calculate the spatial distribution of SW, which can be represented as a superposition of the eigenmodes with wave numbers Φ_{S_1} , Φ_{AS} , and Φ_{S_2} , obtained previous: $|\Psi| = \sum (\Psi_{S_1} e^{i\Phi_{S_1}x} + \Psi_{AS} e^{i\Phi_{AS}x} + \Psi_{S_2} e^{i\Phi_{S_2}x})$, where Ψ_{S_1} , Ψ_{S_2} , Ψ_{AS} are the values of amplitude of the eigenmodes obtained in Figs. 5(a)–5(c). Figures 6(a) and 6(b) show a case of $s = 10 \mu\text{m}$ and Figs. 6(c) and 6(d) show a case of $s = 80 \mu\text{m}$ at $f = 5.3 \text{ GHz}$. It can be seen that as a consequence of dipole lateral and vertical coupling, the spin-wave energy is transferred to the S_2 and S_3 stripes when the S_1 stripe is excited. In the case of $s = 80 \mu\text{m}$, this results in an increase in the coupling length L between the magnetic stripes. If we consider the case of S_3 stripe excitation [see Figs. 6(e) and 6(f)], we observe a redistribution in the spin-wave propagation. The picture is similar to the case of three parallel oriented magnonic stripes [53,59]. Note, however, that in this configuration of spin-wave excitation only the interference of the Φ_{S_1} and Φ_{S_2} modes is taken into account, since the Φ_{AS} mode is not localized in the region of the S_3 stripe. Note that a more detailed description of the case of spin-wave excitation in a stripe S_3 is given in Appendix A.

A key feature of this 3D coupler is the consideration of the geometrical parameters s and d . Figure 6(g) shows how

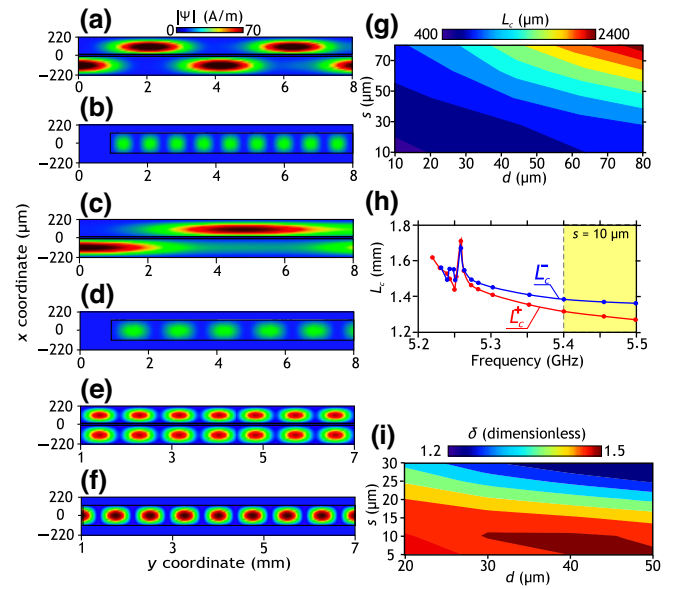


FIG. 6. Spin-wave intensity distributions, case $s = 10 \mu\text{m}$ (a),(b), $s = 80 \mu\text{m}$ (c),(d), and for spin-wave excitation in stripe S_3 (e),(f). (g) Dependence of the coupling length L_c on the values of s and d . The data are given for $B_0 = 120 \text{ mT}$ and input signal frequency $f = 5.3 \text{ GHz}$. (h) Frequency dependence of the coupling length L_c for MSSW propagation in the positive (red curve) and negative (blue curve) directions of the x axis of the 3D coupler. (i) Dependence of the nonreciprocity parameter δ on the values of s and d .

the coupling length L_c depends on the values of s and d . In terms of eigenmodes, the coupling length L_c is calculated as $L_c = 2\pi/|\Phi_{S_1} - \Phi_{S_2}|$ [21,53].

FEM was used to investigate the effect of nonreciprocal SW in the considered structure. Figure 6(h) shows the frequency dependence of the coupling length L_c in the case of MSSW propagation for cases where the B_0 is directed in the negative (blue curve, L_c^-) and positive (red curve, L_c^+) direction of the x axis. It should be noted that the values of coupling lengths obtained by this method are in good agreement with micromagnetic calculations and experimental data. Thus, for the frequency of 5.3 GHz, $L_c = 1.55 \text{ mm}$, with micromagnetic calculation values $L = 1.65 \text{ mm}$, and for BLS measurements— $L = 1.7 \text{ mm}$. It can be seen that in the case of MSSW propagation in the negative direction B_0 relative x axis, an increase in the L_c is observed in the frequency range 5.27–5.5 GHz. In the 5.4 to 5.5 GHz band (see yellow area), the difference between L^- and L^+ is of the order of $200 \mu\text{m}$. The size of the gap s and d between the magnetic stripes must also be taken into account when changing the polarity of the external magnetic field. For this purpose, we introduce a nonreciprocity parameter $\delta = L^-/L^+$, representing the ratio of the coupling lengths in the negative and positive directions of the external magnetic field. Figure 6(i) shows a spatial map of the distribution δ in the range of varying

distances s and d . It can be observed that the maximum value of $\delta = 1.5$ is reached in the range of $s = 5 \dots 10 \mu\text{m}$ and $d = 30 \dots 50 \mu\text{m}$. In terms of the functionality of the proposed coupler, this is a good advantage, as no additional ferroelectric [34,60] or piezoelectric [23] layers are required, since only the polarity of the external magnetic field needs to be changed to change the coupling length.

The fact that the coupling length changes when the polarity of the external magnetic field is reversed can tell us that, as noted in Sec. II, it is not only the presence of an asymmetric internal magnetic field distribution in the magnetic stripes that leads to nonreciprocal spin-wave propagation. The presence of a distributed dipolar coupling in the lateral and vertical directions and hence the overlap integral of the eigenmodes leads to its dependence on the polarity of the external magnetic field.

It is worth noting that the main contribution to the spin-wave energy transfer in this 3D coupler is made by the lateral and vertical coupling coefficients between the magnonic stripes. The lateral coupling coefficient takes into account the distance between S_1 and S_2 , and the vertical coupling coefficient takes into account the distance between S_1 and S_3 as well as S_2 and S_3 . These coefficients can be conventionally called κ_l and κ_v , respectively; a schematic representation of the interaction between the magnonic stripes is shown in Fig. 7(a). If we consider the situation where there are only stripes S_1 and S_3 , and S_3 is also shifted by a distance $\zeta = w/2$ relative to the center of S_1 [see inset in Fig. 7(d)], and plot the H_x -component distribution of the magnetic field [see Fig. 7(b)], we can see that the magnetic field distribution (the \vec{H} direction is indicated by lines with arrows) inside the magnonic stripes is nonuniform in thickness and is also transformed at the stripe edges. The external magnetic field is directed in negative direction of x axis. This fact also causes nonreciprocal propagation of spin waves in the system.

The coupling coefficient in the lateral direction κ_l as a function of the gap value d and the coupling coefficient in the vertical direction κ_v as a function of the shift value between the stripe centers ζ [see the inset in Fig. 7(d)] are shown in Fig. 7(c) by the solid and dashed curves, respectively. It is worth noting that at $\zeta = 0$ the ratio $\kappa_l < \kappa_v$ between the values of the coupling parameters is satisfied when the parameters s and d vary in the range from 10 to 80 μm . Figure 7(d) shows the dependence of κ_v as the value of the shift between the centers of the stripes ζ is varied. It is worthwhile to note that changing the value of ζ from 0 to $w/2$ results in a decrease in the κ_v of 3 cm^{-1} . It can therefore be said that the proposed system has sufficient roughness to change parameters such as the center shift ζ of the magnetic stripe. This allows us to add the dependence of the coefficient κ_v on the polarity of the external magnetic field and to account for the nonreciprocal propagation of spin waves in this model. This is a

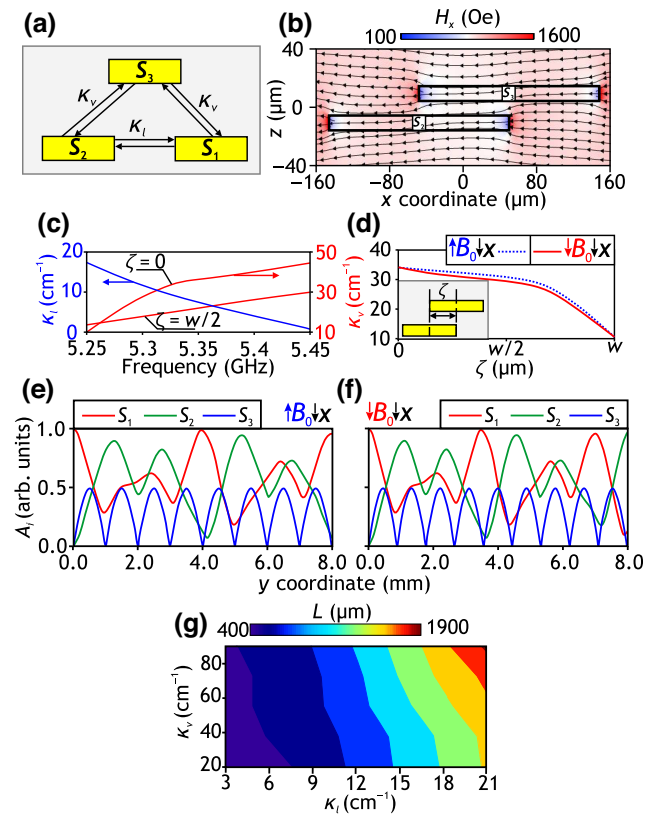


FIG. 7. (a) Sketch of the interaction scheme between magnonic stripes. (b) 2D spatial distribution map of the H_x component of the magnetic field in two magnetic stripes. The arrows indicate the direction of the magnetic field \vec{H} . (c) The lateral coupling coefficient κ_l as a function of the gap value d and the vertical coupling coefficient κ_v as a function of the shear value between the stripe centers ζ are shown as solid and dashed curves, respectively. (d) Dependence of κ_v on the shear between the stripes centres ζ in the positive (blue curve) and negative (red curve) directions of the x axis. (e),(f) Distribution of the spin-wave intensity in the 3D coupler. (g) Dependence of the coupling length L on the values of κ_v and κ_l .

significant advantage over 3D photonic devices [61,62]. By reversing the polarity of the external magnetic field, a slight change in the κ_v values is observed, especially in the region of $\zeta = w/2$. This fact also confirms that in the asymmetric position of the magnetic stripes, the overlap integral of the eigenmodes depends on the direction of the external magnetic field. Figures 7(e) and 7(f) show the solution of the system of Eq. (B1) in Appendix B, we can see that in the stripes the spin-wave intensity redistributes periodically along the stripes $S_{1,2}$ with spatial period $2L$ and oscillates along S_3 with another spatial period. In this case, changing the polarity of the external magnetic field also causes the spin-wave power output port to switch. This also leads to a reduction in the coupling length in the system. Figure 7(g) shows how the coupling length L depends on the values of κ_v and κ_l . Using a combination

of FEM and the solution of Eq. (B4) in Appendix B it is possible to study the influence of geometrical parameters on the value of the spin-wave coupling L .

In contrast to the previously considered multiferroic structures with voltage control [23,34,60], the possibility of which is due to the hybridization of the magneto-static and electromagnetic waves of the ferroelectric layer or using a elastic strains to change a internal magnetic field, the proposed method for controlling the properties of spin waves makes it possible to implement, for example, signal demultiplexing with frequency—spatial selectivity due to the possibility of using reverse an internal magnetic field. Due to similarity of the frequency response from S_3 when the input is S_1 or S_2 the proposed structure could be used as the signal-processing device with constant output from one port in the whole bandwidth. This could be used for magnonic logic application where the case of logic “1” correspond to the state of nonzero signal at the input port of either S_1 or S_2 . The port S_3 remains protected in this case. This is also an advantage over the previously discussed optical [53,61–65] signal coupling and demultiplexing systems, as optical media are isotropic. Unlike photonics, magnonics makes it possible to build micro- [34,66,67] and nanoscale [25,27,68–70] devices with wavelengths in the hundreds of nanometers, and to tune their characteristics by changing the external magnetic field.

V. CONCLUSIONS

Thus, we proposed a three-dimensional magnonic structure based on lateral magnonic stripes with an overlying magnonic stripe. Using micromagnetic modeling and the finite-element method, we obtain the eigenmode spectra of the asymmetric 3D coupler and show that reversal of the external magnetic field polarity leads to coupling between the magnetic stripes. These results suggest that the nonreciprocal propagation of spin waves is manifested in several factors. First, the asymmetric distribution of the internal magnetic field with respect to the center of each magnetic strip. And second, the dependence of the overlap integral of the eigenmodes on the change in polarity of the external magnetic field. Peculiarities of the nonreciprocal propagation of spin waves in the studied structure are revealed. Using Brillouin light-scattering spectroscopy, we have experimentally demonstrated spin-wave transport along the asymmetric 3D coupler. Using experimental techniques, we have investigated the nonreciprocal propagation of spin waves in the considered structure by reversing the polarity of the external magnetic field. Based on the studies, it is shown that in three-dimensional magnonic structures, the magnitude of the spin-wave coupling length decreases, leading to the possibility of increasing the density of functional elements in the design of three-dimensional magnonic networks. The concept of 3D

magnonics can provide increased element density to create scalable and adaptable magnonic networks.

ACKNOWLEDGMENTS

This work was supported by the Russian Science Foundation (Grant No. 23-79-30027).

APPENDIX A: MICROMAGNETIC CALCULATIONS FOR DIFFERENT TYPES OF SPIN-WAVE EXCITATION AND COMPARISON WITH TWO-CHANNEL DIRECTIONAL COUPLER

The main part of the paper dealt mainly with the excitation of spin waves in the magnonic stripe S_1 . This configuration can generally be described as asymmetric, since considering three parallel oriented stripes would imply a case of side stripe rather than central stripe excitation. Thus in this configuration all three eigenmodes (Φ_{S_1} , Φ_{S_2} , $\Phi_{S_{AS}}$) discussed in Sec. IV interfere. In this section, in addition to the results discussed earlier, we consider the case of excitation of spin waves in the magnonic stripe S_2 .

Figures 8(a)–8(h) show the micromagnetic modeling results for the intensity (left panels) and phase (right panels) (m_z component) of the spin waves in the case of S_1 [see Figs. 8(a)–8(d)] and S_3 [see Figs. 8(e)–8(h)] stripes' excitation. When the excitation of the spin waves is carried out on the stripe S_3 [see Figs. 8(e)–8(h)], the picture is similar to the case of three parallel oriented magnetic stripes [23], the spin-wave energy is symmetrically transferred from the stripe S_3 to the stripes S_1 and S_2 . In this case, in contrast to the excitation of the stripe S_1 , there is a significant reduction in the coupling length L by about a factor of 2 (L is indicated in the figures).

Next, we try to estimate the dynamics of the spin-wave propagation as the polarity of the external magnetic field changes. Figures 8(i)–8(k) show the frequency dependencies of the spin-wave output power in the positive (dashed curves) and negative (solid curves) directions of the external magnetic field. Since the symmetry is not broken in this case, the frequency dependence of the output signal is practically identical. In this case, changing the polarity of the external magnetic field only slightly affects the transmission of spin waves through the three-channel 3D magnonic coupler.

It is now necessary to evaluate in more detail the regimes of SW propagation in the proposed asymmetrical coupler, as well as to carry out a comparative analysis with respect to the previously considered configurations of directional couplers [21,25]. Figure 9(a) shows the frequency dependence of the SW power at the output ports P_{out1} , P_{out2} , P_{out3} , corresponding to the stripes S_1 , S_2 , S_3 , respectively. It can be said that the operating range of the asymmetric 3D coupler is 400 MHz within the specified antenna configuration. In this range, we can observe frequency when the

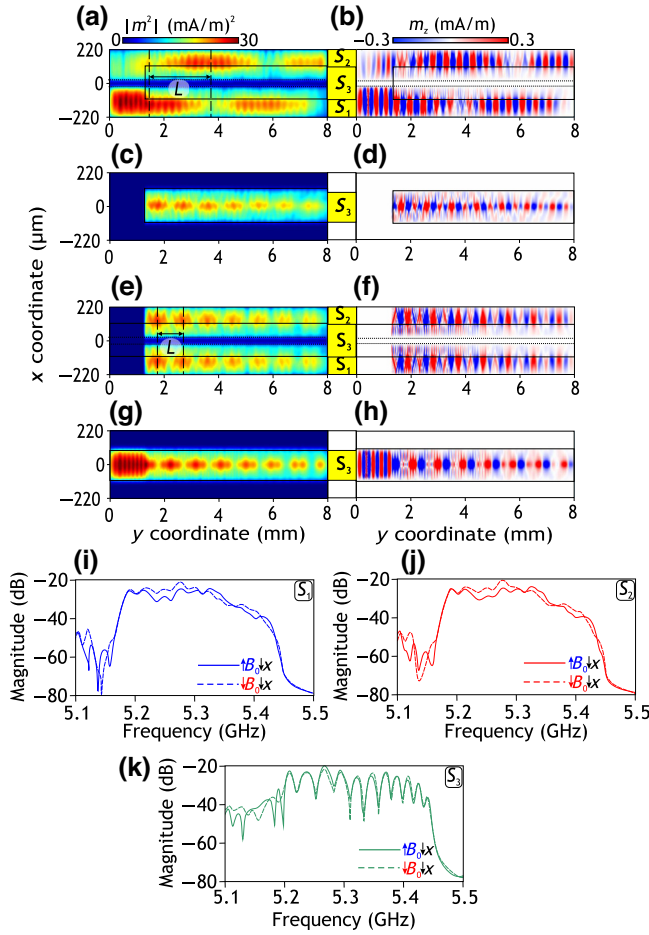


FIG. 8. The left panels show distributions of the spin wave intensity proportional to the magnitude of the square of the dynamic magnetization, the right panels show distributions of the dynamic magnetization component m_z . Cases of exciting stripe S_1 (a)–(d) and stripe S_3 (g)–(h). The data are given for $B_0 = 120$ mT and the input frequency $f = 5.3$ GHz. Frequency dependence of the output power in the stripes S_1 (i), S_2 (j), S_3 (k) for the cases of the external magnetic field direction in the negative direction (solid curves) and positive (dashed curves) direction of the x axis. The excitation of the SWs was carried out in the S_3 stripe.

spin-wave signal comes only from stripe S_1 [see frequency f_1 , in Fig. 9(a)]. At frequency f_2 , a regime is observed where the SW signal comes almost equally from all three stripes. Moving to the high-frequency part of the spectrum, frequency f_3 can be observed and corresponding to the regime where the SW outputs from the S_2 stripe.

As it was already mentioned, in Sec. II of the main part of the paper, it is shown that for a similar coupler geometry, when there is one more YIG stripe above two parallel oriented YIG strips, the phenomenon of nonreciprocal propagation of the SW is observed. Thus, changing the polarity of the external magnetic field leads to a shift of the frequencies $f_{1,2,3}$ [see Fig. 9(b)] and it can be said that

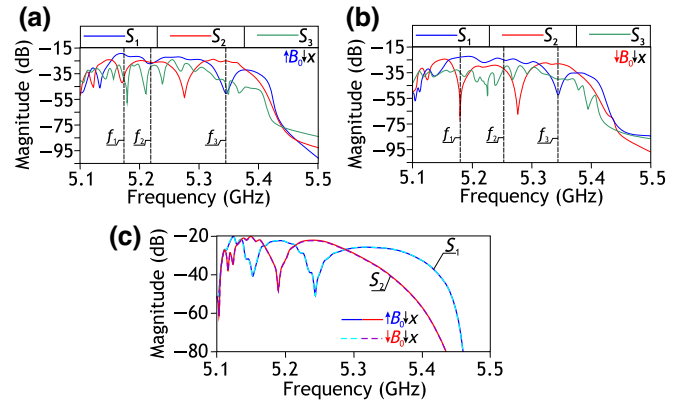


FIG. 9. Frequency dependence of the output power in the stripes S_1 (blue curves), S_2 (red curves), S_3 (green curves) for the cases of the external magnetic field direction in the negative direction (a) and positive (b) direction relative to the x axis. (c) Frequency dependence of the output power in the lateral stripes S_1 and S_2 for the cases of the external magnetic field direction to the negative side (solid curves) and the positive side (dashed curves) relative to the x axis.

the frequency f_2 is strongly shifted and there is a decrease in transmission in stripes S_2 and S_3 at this frequency. At the same time, if we consider the case of two lateral YIG stripes [see Fig. 9(c)], we can see the main difference that in this system there is no nonreciprocal propagation of the SW. Also, the addition of an extra YIG stripe above the lateral stripes leads to the disappearance of the first SW power dip and a shift to the high-frequency region of the second SW power dip in the pass spectrum of stripe S_1 . For stripe S_2 , an additional SW power dip is observed in the high-frequency region.

APPENDIX B: A DESCRIPTION OF THE PHENOMENOLOGICAL MODEL

To account for the intermodal coupling between the magnonic stripes, we write a phenomenological model based on a system of coupled equations in matrix form:

$$-i \frac{d}{dy} \begin{bmatrix} A_1 \\ A_2 \\ A_3 \end{bmatrix} = \begin{bmatrix} \beta_1 & \kappa_l & \kappa_v \\ \kappa_l & \beta_2 & \kappa_v \\ \kappa_v & \kappa_v & \beta_3 \end{bmatrix} \begin{bmatrix} A_1 \\ A_2 \\ A_3 \end{bmatrix}, \quad (\text{B1})$$

where A_i , $i = 1 \dots 3$ is the magnitude of the spin-wave amplitude in the i th stripe, β_i , the propagation constants in the i th isolated stripe, κ_l , κ_v are the lateral and vertical coupling coefficients, respectively. Reorientation of the magnetic field direction results in the variation of κ_v and this will manifest itself in the nonreciprocal behavior of spin-wave power redistribution between three magnonic channels.

Due to the symmetry of the system for the lateral stripes S_1 and S_2 $\beta_1 = \beta_2 = \beta$, for the stripe S_3 we introduce the propagation constant $\beta_3 = \beta + \xi$, where ξ . Let $\beta = 0$, then we go to the system:

$$-i \frac{d}{dy} \begin{bmatrix} A_1 \\ A_2 \\ A_3 \end{bmatrix} = \begin{bmatrix} 0 & \kappa_l & \kappa_v \\ \kappa_l & 0 & \kappa_v \\ \kappa_v & \kappa_v & \xi \end{bmatrix} \begin{bmatrix} A_1 \\ A_2 \\ A_3 \end{bmatrix}. \quad (\text{B2})$$

General solution of the system (B4):

$$\begin{aligned} A_1(z) &= C_1 e^{-jk_l z} + C_2 e^{\frac{jk_l z}{2} + \frac{j\xi z}{2}} \sin\left(\frac{\sqrt{\chi} z}{2}\right) + C_3 e^{\frac{jk_l z}{2} + \frac{j\xi z}{2}} \cos\left(\frac{\sqrt{\chi} z}{2}\right) \\ A_2(z) &= -C_1 e^{-jk_l z} + C_2 e^{\frac{jk_l z}{2} + \frac{j\xi z}{2}} \sin\left(\frac{\sqrt{\chi} z}{2}\right) + C_3 e^{\frac{jk_l z}{2} + \frac{j\xi z}{2}} \cos\left(\frac{\sqrt{\chi} z}{2}\right) \\ A_3(z) &= \frac{e^{\frac{jk_l z}{2} + \frac{j\xi z}{2}}}{2k_v} \left(\left(-j\sqrt{\chi} \cos\left(\frac{\sqrt{\chi} z}{2}\right) + \sin\left(\frac{\sqrt{\chi} z}{2}\right) (\xi - k_l) \right) C_2 \right. \\ &\quad \left. + \left(j\sqrt{\chi} \sin\left(\frac{\sqrt{\chi} z}{2}\right) + \cos\left(\frac{\sqrt{\chi} z}{2}\right) (\xi - k_l) \right) C_3 \right) \end{aligned} \quad (\text{B3})$$

where

$$\chi = \kappa_l^2 - 2\kappa_l \xi + 8\kappa_v^2 + \xi^2 = (\xi - \kappa_l)^2 + 8\kappa_v^2.$$

Let us add boundary conditions when only the magnonic stripes S_1 is excited,

$$A_1(0) = 1, \quad A_2(0) = 0, \quad A_3(0) = 0.$$

A partial solution under given boundary conditions:

$$\begin{aligned} A_1(z) &= \frac{I e^{\frac{1}{2}(\kappa_l + \xi)z} (-\xi + \kappa_l) \sin\left(\frac{\sqrt{\chi} z}{2}\right) + \left(e^{\frac{1}{2}(\kappa_l + \xi)z} \cos\left(\frac{\sqrt{\chi} z}{2}\right) + e^{-I\kappa_l z} \right) \sqrt{\chi}}{2\sqrt{\chi}} \\ A_2(z) &= \frac{I e^{\frac{1}{2}(\kappa_l + \xi)z} (-\xi + \kappa_l) \sin\left(\frac{\sqrt{\chi} z}{2}\right) - \sqrt{\chi} \left(-e^{\frac{1}{2}(\kappa_l + \xi)z} \cos\left(\frac{\sqrt{\chi} z}{2}\right) + e^{-I\kappa_l z} \right)}{2\sqrt{\chi}} \\ A_3(z) &= \frac{2I e^{\frac{1}{2}(\kappa_l + \xi)z} \kappa_v \sin\left(\frac{\sqrt{\chi} z}{2}\right)}{\sqrt{\chi}} \end{aligned} \quad (\text{B4})$$

-
- [1] V. V. Kruglyak, S. O. Demokritov, and D. Grundler, Magnonics, *J. Phys. D: Appl. Phys.* **43**, 264001 (2010).
[2] V. Demidov, S. Urazhdin, G. de Loubens, O. Klein, V. Cros, A. Anane, and S. Demokritov, Magnetization oscillations and waves driven by pure spin currents, *Phys. Rep.* **673**, 1 (2017).
[3] A. Barman, *et al.*, The 2021 magnonics roadmap, *J. Phys.: Condens. Matter* **33**, 413001 (2021).
[4] A. V. Chumak, P. Kabos, M. Wu, C. Abert, C. Adelman, A. O. Adeyeye, J. Akerman, F. G. Aliev, A. Anane, and A. Awad, *et al.*, Advances in magnetics roadmap on spin-wave computing, *IEEE Trans. Magn.* **58**, 1 (2022).

-
- [5] H. Yu, V. Cros, R. Bernard, P. Bortolotti, A. Anane, F. Brandl, F. Heimbach, and D. Grundler, *et al.*, Approaching soft x-ray wavelengths in nanomagnet-based microwave technology, *Nat. Commun.* **7**, 1 (2016).
[6] A. Litvinenko, R. Khymyn, V. Tyberkevych, V. Tikhonov, A. Slavin, and S. Nikitov, Tunable magnetoacoustic oscillator with low phase noise, *Phys. Rev. Appl.* **15**, 034057 (2021).
[7] A. Litvinenko, A. Sidi El Valli, V. Iurchuk, S. Louis, V. Tyberkevych, B. Dieny, A. N. Slavin, and U. Ebels, Ultrafast GHz-range swept-tuned spectrum analyzer with 20 ns temporal resolution based on a spin-torque nano-oscillator with a uniformly magnetized “free” layer, *Nano Lett.* **22**, 1874 (2022).

- [8] A. G. Gurevich and G. A. Melkov, *Magnetization Oscillations and Waves* (CRC-Press, London, New York, 1996).
- [9] D. D. Stancil and A. Prabhakar, *Spin Waves: Theory and Applications* (Springer, New York, 2009).
- [10] A. V. Vashkovskii, V. S. Stal'makhov, and Y. P. Sharaevskii, *Magnetostatic waves in microwave electronics* (Sarat. Gos. Univ., Saratov, 1993), (in Russian).
- [11] P. Graczyk, J. Kłos, and M. Krawczyk, Broadband magnetoelastic coupling in magnonic-phononic crystals for high-frequency nanoscale spin-wave generation, *Phys. Rev. B* **95**, 104425 (2017).
- [12] R. Verba, V. Tiberkevich, and A. Slavin, Spin-wave transmission through an internal boundary: Beyond the scalar approximation, *Phys. Rev. B* **101**, 144430 (2020).
- [13] S. J. Hämäläinen, M. Madami, H. Qin, G. Gubbiotti, and S. van Dijken, Control of spin-wave transmission by a programmable domain wall, *Nat. Commun.* **9**, 1 (2018).
- [14] G. Csaba, Á. Papp, and W. Porod, Perspectives of using spin waves for computing and signal processing, *Phys. Lett. A* **381**, 1471 (2017).
- [15] A. Chumak, A. Serga, and B. Hillebrands, Magnonic crystals for data processing, *J. Phys. D: Appl. Phys.* **50**, 244001 (2017).
- [16] Á. Papp, W. Porod, and G. Csaba, Nanoscale neural network using non-linear spin-wave interference, *Nat. Commun.* **12**, 1 (2021).
- [17] V. Sluka, T. Schneider, R. A. Gallardo, A. Kákay, M. Weigand, T. Warnatz, R. Mattheis, A. Roldán-Molina, P. Landeros, and V. Tiberkevich, *et al.*, Emission and propagation of 1D and 2D spin waves with nanoscale wavelengths in anisotropic spin textures, *Nat. Nanotechnol.* **14**, 328 (2019).
- [18] C. S. Davies, A. V. Sadovnikov, S. V. Grishin, Y. P. Sharaevsky, S. A. Nikitov, and V. V. Kruglyak, Field-controlled phase-rectified magnonic multiplexer, *IEEE Trans. Magn.* **51**, 3401904 (2015).
- [19] A. Sadovnikov, V. Gubanov, S. Sheshukova, Y. P. Sharaevskii, and S. Nikitov, Spin-wave drop filter based on asymmetric side-coupled magnonic crystals, *Phys. Rev. Appl.* **9**, 051002 (2018).
- [20] P. Gruszecki, K. Y. Guslienko, I. L. Lyubchanskii, and M. Krawczyk, Inelastic spin-wave beam scattering by edge-localized spin waves in a ferromagnetic thin film, *Phys. Rev. Appl.* **17**, 044038 (2022).
- [21] A. V. Sadovnikov, E. N. Beginin, S. E. Sheshukova, D. V. Romanenko, Y. P. Sharaevskii, and S. A. Nikitov, Directional multimode coupler for planar magnonics: Side-coupled magnetic stripes, *Appl. Phys. Lett.* **107**, 202405 (2015).
- [22] Q. Wang, A. Hamadeh, R. Verba, V. Lomakin, M. Mohseni, B. Hillebrands, A. V. Chumak, and P. Pirro, Author correction: A nonlinear magnonic nano-ring resonator, *npj Comput. Mater.* **7**, 26 (2021).
- [23] A. Sadovnikov, A. Grachev, S. Sheshukova, Y. P. Sharaevskii, A. Serdobintsev, D. Mitin, and S. Nikitov, Magnon straintronics: Reconfigurable spin-wave routing in strain-controlled bilateral magnetic stripes, *Phys. Rev. Lett.* **120**, 257203 (2018).
- [24] A. Sadovnikov, E. Beginin, S. Odincov, S. Sheshukova, Y. P. Sharaevskii, A. Stognij, and S. Nikitov, Frequency selective tunable spin wave channeling in the magnonic network, *Appl. Phys. Lett.* **108**, 172411 (2016).
- [25] Q. Wang, A. V. Chumak, and P. Pirro, Inverse-design magnonic devices, *Nat. Commun.* **12**, 2636 (2021).
- [26] A. Sadovnikov, S. Odintsov, E. Beginin, S. Sheshukova, Y. P. Sharaevskii, and S. Nikitov, Toward nonlinear magnonics: Intensity-dependent spin-wave switching in insulating side-coupled magnetic stripes, *Phys. Rev. B* **96**, 144428 (2017).
- [27] Q. Wang, M. Kewenig, M. Schneider, R. Verba, F. Kohl, B. Heinz, M. Geilen, M. Mohseni, B. Lägel, and F. Ciubotaru, *et al.*, A magnonic directional coupler for integrated magnonic half-adders, *Nat. Electron.* **3**, 765 (2020).
- [28] E. Beginin, A. Sadovnikov, A. Y. Sharaevskaya, A. Stognij, and S. Nikitov, Spin wave steering in three-dimensional magnonic networks, *Appl. Phys. Lett.* **112**, 122404 (2018).
- [29] F. Heussner, A. Serga, T. Brächer, B. Hillebrands, and P. Pirro, A switchable spin-wave signal splitter for magnonic networks, *Appl. Phys. Lett.* **111**, 122401 (2017).
- [30] Y. Khivintsev, V. Sakharov, A. Kozhevnikov, G. Dudko, Y. Filimonov, and A. Khitun, Spin waves in YIG based magnonic networks: Design and technological aspects, *J. Magn. Magn. Mater.* **545**, 168754 (2022).
- [31] F. Heussner, G. Talmelli, M. Geilen, B. Heinz, T. Brächer, T. Meyer, F. Ciubotaru, C. Adelman, K. Yamamoto, and A. A. Serga, *et al.*, Experimental realization of a passive gigahertz frequency-division demultiplexer for magnonic logic networks, *Phys. Status Solidi RRL* **14**, 1900695 (2020).
- [32] S. Pan, S. Mondal, M. Zelent, R. Szwiercz, S. Pal, O. Hellwig, M. Krawczyk, and A. Barman, Edge localization of spin waves in antidot multilayers with perpendicular magnetic anisotropy, *Phys. Rev. B* **101**, 014403 (2020).
- [33] K. Szulc, P. Graczyk, M. Mruczkiewicz, G. Gubbiotti, and M. Krawczyk, Spin-wave diode and circulator based on unidirectional coupling, *Phys. Rev. Appl.* **14**, 034063 (2020).
- [34] A. V. Sadovnikov, A. A. Grachev, E. N. Beginin, S. E. Sheshukova, Y. P. Sharaevskii, and S. A. Nikitov, Voltage-controlled spin-wave coupling in adjacent ferromagnetic-ferroelectric heterostructures, *Phys. Rev. Appl.* **7**, 014013 (2017).
- [35] Y. Hu, B. T. Miles, Y.-L. D. Ho, M. P. Taverne, L. Chen, H. Gersen, J. G. Rarity, and C. F. Faul, Toward direct laser writing of actively tuneable 3D photonic crystals, *Adv. Opt. Mater.* **5**, 1600458 (2017).
- [36] R. Kubrin, R. M. Pasquarelli, M. Waleczek, H. S. Lee, R. Zierold, J. J. do Rosário, P. N. Dyachenko, J. M. Montero Moreno, A. Y. Petrov, and R. Janssen, *et al.*, Bottom-up fabrication of multilayer stacks of 3D photonic crystals from titanium dioxide, *ACS. Appl. Mater. Interfaces* **8**, 10466 (2016).
- [37] P. Popov, A. Y. Sharaevskaya, E. Beginin, A. Sadovnikov, A. Stognij, D. Kalyabin, and S. Nikitov, Spin wave propagation in three-dimensional magnonic crystals and coupled structures, *J. Magn. Magn. Mater.* **476**, 423 (2019).
- [38] G. Gubbiotti, *Three-Dimensional Magnonics: Layered, Micro-And Nanostructures* (CRC Press, New York, 2019).

- [39] S. Sahoo, A. May, A. van Den Berg, A. K. Mondal, S. Ladak, and A. Barman, Observation of coherent spin waves in a three-dimensional artificial spin ice structure, *Nano Lett.* **21**, 4629 (2021).
- [40] P. A. Grünberg, Nobel lecture: From spin waves to giant magnetoresistance and beyond, *Rev. Mod. Phys.* **80**, 1531 (2008).
- [41] M. Jamali, J. H. Kwon, S.-M. Seo, K.-J. Lee, and H. Yang, Spin wave nonreciprocity for logic device applications, *Sci. Rep.* **3**, 1 (2013).
- [42] J. Chen, H. Yu, and G. Gubbiotti, Unidirectional spin-wave propagation and devices, *J. Phys. D: Appl. Phys.* **55**, 123001 (2021).
- [43] H. Wang, J. Chen, T. Yu, C. Liu, C. Guo, S. Liu, K. Shen, H. Jia, T. Liu, and J. Zhang, *et al.*, Nonreciprocal coherent coupling of nanomagnets by exchange spin waves, *Nano Res.* **14**, 2133 (2021).
- [44] P. Deorani, J. H. Kwon, and H. Yang, Nonreciprocity engineering in magnetostatic spin waves, *Curr. Appl. Phys.* **14**, S129 (2014).
- [45] O. Gladii, M. Haidar, Y. Henry, M. Kostylev, and M. Bailleul, Frequency nonreciprocity of surface spin wave in permalloy thin films, *Phys. Rev. B* **93**, 054430 (2016).
- [46] F. Vanderveken, H. Ahmad, M. Heyns, B. Sorée, C. Adelman, and F. Ciubotaru, Excitation and propagation of spin waves in non-uniformly magnetized waveguides, *J. Phys. D: Appl. Phys.* **53**, 495006 (2020).
- [47] P. Gerevenkov, I. A. Filatov, A. Kalashnikova, and N. Khokhlov, Unidirectional propagation of spin waves excited by femtosecond laser pulses in a planar waveguide, *Phys. Rev. Appl.* **19**, 024062 (2023).
- [48] S. Odintsov, S. Sheshukova, S. Nikitov, E. Lock, E. Beginin, and A. Sadovnikov, Nonreciprocal spin wave propagation in bilayer magnonic waveguide, *J. Magn. Magn. Mater.* **546**, 168736 (2022).
- [49] S. Seki, Y. Okamura, K. Kondou, K. Shibata, M. Kubota, R. Takagi, F. Kagawa, M. Kawasaki, G. Tatara, and Y. Otani, *et al.*, Magnetochiral nonreciprocity of volume spin wave propagation in chiral-lattice ferromagnets, *Phys. Rev. B* **93**, 235131 (2016).
- [50] T. O'keeffe and R. Patterson, Magnetostatic surface-wave propagation in finite samples, *J. Appl. Phys.* **49**, 4886 (1978).
- [51] L. D. Landau and E. M. Lifschitz, On the theory of the dispersion of magnetic permeability in ferromagnetic bodies, *Phys. Z. Sowjet.* **8**, 153 (1935).
- [52] A. Vansteenkiste, J. Leliaert, M. Dvornik, M. Helsen, F. Garcia-Sanchez, and B. Van Waeyenberge, The design and verification of mumax3, *AIP Adv.* **4**, 107133 (2014).
- [53] R. J. McCosker and G. E. Town, Multi-channel directional coupler as an evanescent field optical sensor, *Sens. Actuators, B* **150**, 417 (2010).
- [54] G. Venkat, D. Kumar, M. Franchin, O. Dmytriiev, M. Mruczkiewicz, H. Fangohr, A. Barman, M. Krawczyk, and A. Prabhakar, Proposal for a standard micromagnetic problem: Spin wave dispersion in a magnonic waveguide, *IEEE Trans. Magn.* **49**, 524 (2013).
- [55] M. Krawczyk and D. Grundler, Review and prospects of magnonic crystals and devices with reprogrammable band structure, *J. Phys.: Condens. Matter* **26**, 123202 (2014).
- [56] S. Demokritov, B. Hillebrands, and A. Slavin, Brillouin light scattering studies of confined spin waves: Linear and nonlinear confinement, *Phys. Rep.* **348**, 441 (2001).
- [57] S. O. Demokritov and V. E. Demidov, Micro-Brillouin light scattering spectroscopy of magnetic nanostructures, *IEEE Trans. Magn.* **44**, 6 (2008).
- [58] V. E. Demidov and S. O. Demokritov, Magnonic waveguides studied by microfocus Brillouin light scattering, *IEEE Trans. Magn.* **51**, 1 (2015).
- [59] A. Grachev, S. Sheshukova, M. Kostylev, S. Nikitov, and A. Sadovnikov, Reconfigurable dipolar spin-wave coupling in a bilateral yttrium iron garnet structure, *Phys. Rev. Appl.* **19**, 054089 (2023).
- [60] V. E. Demidov, B. A. Kalinikos, S. F. Karmanenko, A. A. Semenov, and P. Edenhofer, Electrical tuning of dispersion characteristics of surface electromagnetic-spin waves propagating in ferrite-ferroelectric layered structures, *IEEE Trans. Microw. Theory Tech.* **51**, 2090 (2003).
- [61] S. Yoo, B. Guan, and R. P. Scott, Heterogeneous 2D/3D photonic integrated microsystems, *Microsyst. Nanoeng.* **2**, 1 (2016).
- [62] X. Mu, S. Wu, L. Cheng, and H. Fu, Edge couplers in silicon photonic integrated circuits: A review, *Appl. Sci.* **10**, 1538 (2020).
- [63] C. J. Brooks, A. P. Knights, and P. E. Jessop, Vertically-integrated multimode interferometer coupler for 3D photonic circuits in SOI, *Opt. Express* **19**, 2916 (2011).
- [64] K. Shang, S. Pathak, B. Guan, G. Liu, and S. Yoo, Low-loss compact multilayer silicon nitride platform for 3D photonic integrated circuits, *Opt. Express* **23**, 21334 (2015).
- [65] H. Gao, G. F. Chen, P. Xing, J. W. Choi, H. Y. Low, and D. T. Tan, High-resolution 3D printed photonic waveguide devices, *Adv. Opt. Mater.* **8**, 2000613 (2020).
- [66] A. V. Sadovnikov, S. Davies, S. V. Grishin, V. V. Kruglyak, D. V. Romanenko, Y. P. Sharaevskii, and S. A. Nikitov, Magnonic beam splitter: The building block of parallel magnonic circuitry, *Appl. Phys. Lett.* **106**, 192406 (2015).
- [67] A. Martyshkin, C. Davies, and A. Sadovnikov, Magnonic interconnections: Spin-wave propagation across two-dimensional and three-dimensional junctions between yttrium iron garnet magnonic stripes, *Phys. Rev. Appl.* **18**, 064093 (2022).
- [68] H. Qin, R. B. Holländer, L. Flajšman, F. Hermann, R. Dreyer, G. Woltersdorf, and S. van Dijken, Nanoscale magnonic Fabry-Pérot resonator for low-loss spin-wave manipulation, *Nat. Commun.* **12**, 2293 (2021).
- [69] N. Träger, P. Gruszecki, F. Lisiecki, F. Groß, J. Förster, M. Weigand, H. Głowiński, P. Kuświk, J. Dubowik, and M. Krawczyk, *et al.*, Demonstration of k -vector selective microscopy for nanoscale mapping of higher order spin wave modes, *Nanoscale* **12**, 17238 (2020).
- [70] A. A. Grachev, A. V. Sadovnikov, and S. A. Nikitov, Strain-tuned spin-wave interference in micro- and nanoscale magnonic interferometers, *Nanomaterials* **12**, 1520 (2022).